

NANOINDENTATION AND CRYSTAL PLASTICITY FINITE ELEMENT ANALYSIS OF PROTON AND HELIUM IRRADIATED ALLOY 800H

Qiang Wang[✉], Zhouyao Wang, Yuqing Ding, Vineet Bhakhri

Canadian Nuclear Laboratories, Chalk River, Ontario, Canada ✉ Qiang.wang@cnl.ca

ABSTRACT

Proton and helium irradiated Alloy 800H material was characterized using nanoindentation and transmission electron microscopy (TEM). The material was irradiated by a 1.5 MeV proton beam followed by helium implantation to 7000 appm at 700 °C. The He implantation was carried out using an ion beam energy degrader and a relatively homogenous distribution of helium was achieved for up to 10 μm . The irradiated and non-irradiated materials were characterized using nanoindentation and significant irradiation hardening was detected. Transmission electron microscopy showed the formation of dislocation loops, He bubbles, and Ti-rich precipitation due to irradiation, which were thought to contribute to the irradiation hardening phenomenon. A crystal plasticity finite element model (CPFEM) was developed to simulate nanoindentation. The model was able to reproduce the experiment results and provide reasonable predictions for the effect of irradiation on plastic deformation.

INTRODUCTION

The excellent high temperature creep and corrosion resistance of Alloy 800H make it a potential candidate for Gen IV reactors like the Very High-Temperature Reactor (VHTR) and Gas-cooled Fast Reactor (GFR) (Rowcliffe et al. 2009). However, Ni-based structural materials, including Alloy 800H, are typically susceptible to helium embrittlement during nuclear applications. Helium atoms, resulting from the (n, α) transmutation reaction, tend to form He bubbles, especially at high temperatures, which can potentially degrade the mechanical properties of the materials (Wang et al. 2022). Apart from helium bubbles, irradiation induced damage significantly influence the mechanical properties of the material. Gan et al. (Gan et al. 2006) first reported the microstructure changes of 800H induced by 5 MeV Ni ion irradiation up to 50 dpa at 500 °C. The irradiated microstructure exhibited both perfect and faulted dislocation loops. Nanstad et al. (Nanstad et al. 2009) tested the Alloy 800H material after irradiation in the High-Flux Isotope Reactor (HFIR) at temperatures from about 550 to 700 °C, and to doses about 1.2-1.6 dpa. Irradiation at 580 °C induced significant increase in yield strength and UTS by 100% and 50%, respectively. Less irradiation hardening was found in the material irradiated at 660 °C. However, due to a lack of characterization on the microstructure, the relationship between irradiation-induced damage, cavities, and mechanical properties was not well-established. Recently, Zhu et al. (Zhu et al. 2022) reported irradiation induced hardening in a 3 MeV Cu ion irradiated 800H at room temperature. The maximum nanoindentation depth in their experiment was 200 nm. The authors revealed the irradiated microstructure and reported that the irradiated samples possessed higher geometrically necessary dislocations (GND) than the non-irradiated material. The effects of the GND and irradiation-induced damage on hardness were, however, difficult to separate. Therefore, more representative mechanical measurement on the irradiated sample is still lacking.

Nanoindentation has been proven to be highly valuable for studying accelerated ion irradiated materials, where the thickness of the irradiated layer typically ranges from only a few hundred nanometers to a few tens of micrometers (Hardie, Roberts, and Bushby 2015; Hosemann et al. 2009; Was 2015). However, the results obtained from nanoindentation are often not directly comparable to those from standard tests, e.g., uniaxial tensile test. Due to the complexity in interpreting nanoindentation results,

hardness measurement represents just the initial step in understanding the effect of irradiation on mechanical properties. To address this challenge, researchers have proposed a variety of methods to deduce more general properties, such as yield strength or work hardening properties, from nanoindentation results (Bouzakis and Michailidis 2006; Pathak and Kalidindi 2015; Wang et al. 2018). Crystal plasticity finite element modeling (CPFEM) is commonly employed to simulate or validate the nanoindentation experiment data (Lin, Nie, and Liu 2020; Xia et al. 2014; Zaafarani et al. 2006). However, the implementation of CPFEM typically relies on commercial finite element software, e.g., MARC (Zaafarani et al. 2006) and ABAQUS (Xia et al. 2014)(Lin, Nie, and Liu 2020), and the implementation in an open source platform would make CPFEM more accessible for research applications.

In this work, the microstructure of the proton and helium irradiated Alloy 800H was characterized using Transmission Electron Microscopy (TEM), providing valuable insights into the mechanical performance of the material during nanoindentation test. We also present a CPFEM-assisted nanoindentation investigation based on an open-source finite element code, WARP3D (Healy et al. 2022). A procedure for calculating yield strengths based on nanoindentation results and incorporate these values into the model is demonstrated.

EXPERIMENTS AND MODELING

Material and Irradiation

The Alloy 800H material used in the current research was supplied by American Special Metals, Corp., Florida, USA (American Special Metals n.d.). The average grain size is approximately 120 μm based on the electron backscatter diffraction (EBSD) measurement. A sample with an approximate size of 10 mm in length and 6 mm in width was irradiated at 700 $^{\circ}\text{C}$ by a 1.5 MeV proton beam followed by He implantation to 7000 appm at the same temperature at the Reactor Materials Testing Laboratory (RM TL) at Queen's University, Canada. The damage profile simulated by the Stopping and Range of Ions in Matter (SRIM) code using the Kinchin–Pease mode (Stoller et al. 2013) is shown in Figure 1 and the damage in the plateau region was approximately 1 dpa. The dose rate in the plateau region was approximately 0.77×10^{-5} dpa/s. By accommodating the dose rate effect by temperature shift (WAS 2017), assuming the dose rate of neutron irradiation is approximately two orders of magnitude lower than that of proton irradiation (Was 2015), the proton irradiated microstructure at 700 $^{\circ}\text{C}$ emulates that of 610 $^{\circ}\text{C}$ from neutron irradiation. The He implantation was achieved through an ion beam energy degrader (Topping et al. 2023). In this experiment, 12 foils with the thickness ranging from 60 to 82 μm with 2 μm intervals were used to generate a depth of approximately 10 μm with relative homogenous distribution of helium. The profile of the helium composition distribution is also plotted in Figure 1. The fluctuations in the composition curve are due to the limited number of foils employed. The deviation of the composition can be found as 7000 ± 1000 appm. The irradiation plan was to use 14 foils, but the final two foils were interrupted and not completed. The damage dose induced by helium implantation is only approximately 0.02 dpa for each depth, which is much smaller than the dose induced by the proton irradiation. Therefore, the final dose of the samples received was determined by the proton irradiation.

Nanoindentation

The nanoindentation experiment was carried out at room temperature using the NanoTest Vantage nanoindenter. For each indent, the Berkovich indenter was loaded to 300 mN through 10 loading-partial unloading cycles at a constant rate of 0.1 per second. In each cycle, except for the last one, the indenter was unloaded to 80% of the current maximum load at a rate of 10 mN/s. The indenter was held at the maximum load for 5 seconds before fully unloaded. A total of 8 indents were tested for each sample and the indents were spaced by 100 μm .

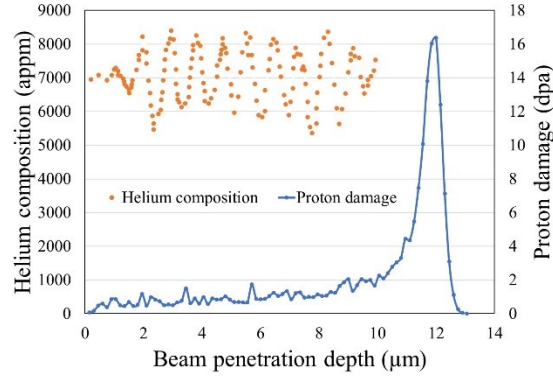


Figure 1 Damage profile of 1.5 MeV proton irradiation and the composition profile of the implanted helium.

TEM characterization

Transmission Electron Microscopy (TEM) was employed to study the microstructure of the irradiated material using JEOL F200 multi-purpose electron microscope. The TEM sample from the non-irradiated material was prepared using the dual-stream electro-polishing method using 10% perchloric methanol solution at -40 °C. The TEM sample from the irradiated material was prepared using a FEI Versa 3D Focused Ion Beam (FIB).

CPFEM

The Crystal plasticity finite element modelling (CPFEM) was carried out using the open-source finite element code WARP3D (Healy et al. 2022). In the current research, the Mechanical Threshold Stress (MTS) model was selected to describe the material plasticity behaviour. The MTS model takes into consideration the temperature and the rate dependent hardening in Stage III of the work hardening process. A brief description of the MTS model embedded in WARP3D is as follows.

In the MTS model, the shear strength of one slip system, $\tilde{\tau}$, is written as:

$$\tilde{\tau} = \tau_a + \tau_y(T, \dot{\epsilon}) \frac{\mu(T)}{\mu_0} + \bar{\tau}(\epsilon_p, T, \dot{\epsilon}) \frac{\mu(T)}{\mu_0} \quad (1)$$

where, τ_a and τ_y represent the temperature (T) and strain rate ($\dot{\epsilon}$) invariant and variant components of the yield stress, respectively, and $\bar{\tau}$ represents the increase in strength due to forest dislocation hardening. The $\mu(T)/\mu_0$ ratio describes the temperature dependent elastic properties. Additionally, $\bar{\tau}$, which adopted a form of Voce hardening, is described by Equation 2.

$$\frac{d\bar{\tau}}{dt} = \theta_0 \left(1 - \frac{\bar{\tau}}{\tau_v(T, \dot{\epsilon})} \right)^m \sum_{\alpha=1}^{n_{slip}} |\dot{\gamma}^\alpha| \quad (2)$$

Where, θ_0 is the initial strength at the start of Stage III, τ_v defines the saturation strength of work hardening for a given temperature and rate with no dependence on accumulated plastic strain. $\sum |\dot{\gamma}^\alpha|$ is the accumulated plastic strain rate of all slip systems.

$\tau_y(T, \dot{\epsilon})$ and $\tau_v(T, \dot{\epsilon})$ are described by the following equations adopting an Arrhenius-type law to scale the mechanical threshold to a specified combination of rate and temperature.

$$\tau_y(T, \dot{\epsilon}) = \hat{\tau}_y \left[1 - \left(\frac{kT}{\mu(T)b^3 g_{0,y}} \ln \frac{\dot{\epsilon}_{0,y}}{\dot{\epsilon}} \right)^{\frac{1}{q_y}} \right]^{\frac{1}{p_y}} \quad (3)$$

$$\tau_v(T, \dot{\epsilon}) = \hat{\tau}_v \left[1 - \left(\frac{kT}{\mu(T)b^3 g_{0,v}} \ln \frac{\dot{\epsilon}_{0,v}}{\dot{\epsilon}} \right)^{\frac{1}{q_v}} \right]^{\frac{1}{p_v}} \quad (4)$$

$$\dot{\epsilon} = \sqrt{\frac{2}{3}} D:D \quad (5)$$

where k is the Boltzmann constant, T is the absolute temperature, b is the magnitude of the Burger's vector, $g_{0,y}$ and $g_{0,v}$ are normalized activation energies, $\dot{\epsilon}_{0,(y,v)}$ are reference strain rates, and $q_{(y,v)}$, $p_{(y,v)}$ are constants related to the shape of the activation energy barrier. $\hat{\tau}_y$ and $\hat{\tau}_v$ describe the strength at 0 K associated with yield and work hardening mechanisms, respectively. $\dot{\epsilon}$ is the strain rate obtained through the symmetric part of the spatial velocity gradient, D .

The temperature dependence of shear modulus is given by:

$$\mu(T) = \mu_0 - \frac{D_0}{\exp(T_0/T) - 1} \quad (6)$$

where μ_0 and D_0 are constants and T_0 is the reference temperature.

The mesh of a three-dimensional finite element nanoindentation model of the specimen was achieved using the MATLAB toolkit "STABiX" (Mercier et al. 2015). More specifically, the specimen, set as deformable with 30 μm in height and 60 μm in diameter, was discretized by 23104 8-node hexahedral elements. A mesh convergence study was conducted to assure sufficient accuracy of the model. Given the maximum nanoindentation depth was approximately 2.5 μm , the height of the model is large enough to avoid the influence from the substrate. Nodal displacements were fixed on the bottom and outer surfaces.

WARP3D can only handle contacts between a deformable mesh and a set of rigid contact surfaces. Additionally, only three types of geometries of rigid contact surfaces, i.e., rectangular surfaces, cylinders, and spheres, are supported. The description of a contact surface requires a specification of the type of the surface, the geometry, the orientation in space, and the parameters stiffness, velocity, etc. In WARP3D, a surface can be defined by two vectors that are constructed by three points as shown in Figure 2 (a). The normal vector $v_3 = v_1 \times v_2$ defines the positive (outward) side of the surface, i.e., the contact plane. In the model, the triangle-shaped surfaces of the Berkovich indenter were represented by six rectangular surfaces, each of which was constructed out of three nodes as shown in Figure 2 (b). For instance, the side surface P1-P3-P4 consists of Surface 1 (P1, P2, P3) and Surface 2 (P1, P4, P5). Inevitably, Surface 1 and 2 will overlap. However, since the normal vectors of the two surfaces are the same, no effects were caused on the simulation results. The contact surface was set as frictionless.

It is worth noting that the simulation did not simulate the intermittent loading-unloading steps in order to improve the modelling economy and efficiency. Alternatively, the indenter in our model was directly loaded to the desired depth followed by unloading. The loading and unloading processes for the simulation were both controlled by the same constant displacement rates of 10 nm/s, which was comparable to the experimental condition.

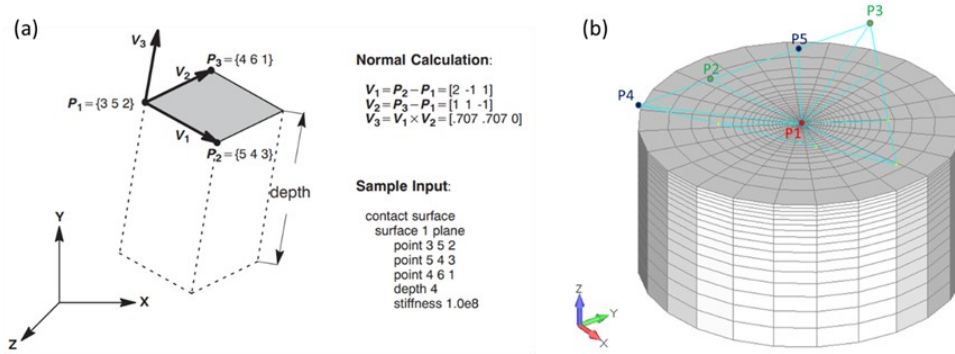


Figure 2 (a) Definition of a rectangular contact surface in WARP3D, (b) schematic demonstration of the construction of the Berkovich indenter in WARP3D.

RESULTS AND DISCUSSION

Nanoindentation

The nanoindentation load-displacement results for both non-irradiated and irradiated samples are displayed in Figure 3 (a). The maximum displacement decreased after irradiation, indicating an increase in hardness. Since the nanoindentation measurement is usually subject to indentation size effect (ISE), the multi-cycle results were further analysed using the Nix-Gao model (Nix and Gao 1998) to calculate the intrinsic hardness at a nominally infinite depth, H_0 . The results are plotted in Figure 3 (b). The hardness of the non-irradiated and irradiated sample were calculated to be 1.72 ± 0.01 GPa and 2.66 ± 0.01 GPa, respectively, representing a 54.65% increase due to irradiation. The average reduced modulus of the non-irradiated and irradiated samples were 178.15 ± 10.41 GPa and 185.76 ± 12.31 GPa, respectively, indicating negligible change to the elastic property by the irradiation. The irradiation-induced hardness increment has also been reported in literature (Prasitthipayong et al. 2018) (Zhu et al. 2022). Prasitthipayong et al. (Prasitthipayong et al. 2018) found that the hardness of Alloy 800H irradiated with Fe ions increased from ~ 2.1 GPa to ~ 3.5 GPa after a total dose of 20.68 dpa. Since it was measured in the entire damage layer and the damage profile from the heavy ion irradiation was not as uniform as the proton irradiation, the reported dose of Prasitthipayong et al. was likely overestimated, especially for the characterized region by nanoindentation.

Subsequently, the hardness was converted to yield strength to compare with other literature results. Toloczko et al. (Toloczko et al. 2018) demonstrated that the yield strength of austenitic steels can be correlated to the Vickers hardness, H_V , using a linear relationship:

$$\sigma_y \text{ [MPa]} = 2.69 H_V \text{ [kg/mm}^2\text{]} - 125 \quad (7)$$

H_V is typically calculated using the contact surface area and it can be converted to the Vickers hardness, H_V^c , calculated from the projected area through a factor (Takayama et al. 2013), i.e., $H_V^c = 0.01058 H_V$. Since H_V^c is approximately close to H_0 (Takayama et al. 2013), Equation 7 can be rewritten as:

$$\sigma_y \text{ [MPa]} = \frac{2.69}{0.01058} H_0 \text{ [GPa]} - 125 \quad (8)$$

Based on Equation 8, the yield strength of the non-irradiated and irradiated samples was calculated as 312.31 ± 2.55 and 551.31 ± 2.55 MPa, respectively. The calculated yield strength for the non-irradiated material is close to the data from the supplier (American Special Metals n.d.) and literature (Tan et al. 2019). For instance, Tan et al. (Tan et al. 2019) reported the yield strength of Alloy 800H as 272 MPa at room temperature. Notably, Nanstad et al. (Nanstad et al. 2009) reported that the yield strength of Alloy

800H increased from 263.2 MPa to between 540.9 and 567.7 MPa after it was irradiated at 580 °C to 1.28 dpa in the ORNL High-Flux Isotope Reactor (HFIR).

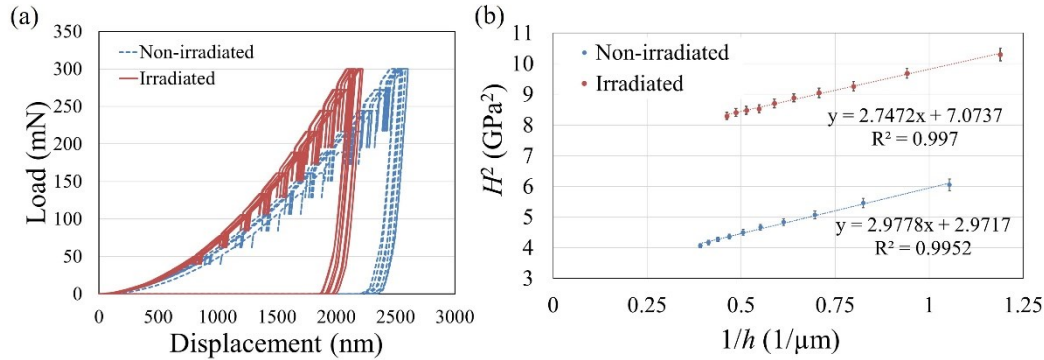


Figure 3 (a) Displacement-load results of the nanoindentation, (b) Depth dependence of hardness, plotted as H^2 versus $1/h$, and fitted by the Nix-Gao model.

CPFEM

To validate the calculated yield strength from nanoindentation and obtain further insights into the material deformation properties, the nanoindentation experiment was simulated using the WARP3D CPFEM code (Healy et al. 2022).

Table 1 summarizes the input parameters for the MTS model (Follansbee and Kocks 1988), which was selected to describe the material property. The Stage II strain hardening rate, θ_0 , was assumed to be 1/200 of the shear modulus (Kocks and Mecking 2003). According to Ref. (Stoller and Zinkle 2000), the critical resolved shear stress can be calculated through dividing the yield strength by the Taylor factor, 3.06. In the framework of WARP3D, the yield strength equals $\tau_a + \tau_y(T, \dot{\epsilon})$ (see Equation 1). Since τ_a is the athermal component of the yield strength and it is dependent on the Hall-Petch effect (Banerjee 2007), it was assumed that τ_a equals 0 in this work due to single crystal indentation. Therefore, $\tau_y(T, \dot{\epsilon})$ for the non-irradiated and irradiated samples are 102 MPa and 176 MPa, respectively. $\hat{\tau}_y$ and $\hat{\tau}_v$ in Equation 3 and 4 represent the strength at 0K associated with yield and work hardening mechanisms, respectively. However, the real values are not obtainable. In the simulation, however, it is the value of $\tau_y(T, \dot{\epsilon})$ that is directly employed. Given the values of $\tau_y(T, \dot{\epsilon})$, through adopting empirical values for $g_{0,y}$, q_y , and p_y in Equation 3 from literature (Kocks and Mecking 2003) (Banerjee 2007), $\hat{\tau}_y$ can be decided to be 123 MPa and 207 MPa, for the non-irradiated and irradiated samples, respectively. Therefore, the values of $\hat{\tau}_y$ may not reflect the real strength of the material at 0K, but this will not affect the simulation results. Using the empirical values for $g_{0,v}$, q_v , and p_v from literature (Kocks and Mecking 2003), $\hat{\tau}_v$ was subsequently optimized through an iterative process. Default values were kept for the rest of the parameters including n , m , D_0 , which represent the hardening exponent, Voce hardening parameter, and temperature dependence constant, respectively.

The simulated load-displacement curves for the non-irradiated and irradiated conditions are shown in Figure 4. The simulated loading curves are within the deviation of the experimental curves, indicating a good agreement between the simulation and experiment results. The calculated hardness from the single-depth simulation results for the non-irradiated and irradiated samples are 2.18 GPa and 3.06 GPa, respectively. For a direct comparison, the hardness, calculated based on the last unloading during experiment, are 2.02 GPa and 2.88 GPa for non-irradiated and irradiated samples, respectively. The simulation results are slightly higher than experiment is because that the creep deformation during the

5-second holding period was not considered in the simulation. As a result, the simulated residual depths are slightly shallower than experiment as shown in Figure 4.

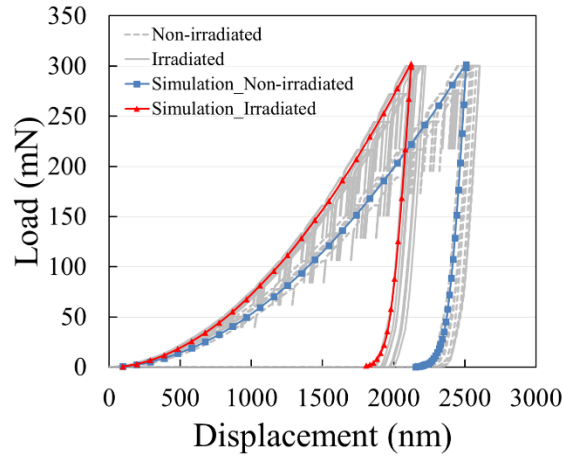


Figure 4 Simulated load-displacement curves.

Table 1 Input Parameters for the MTS Model

Parameter	Value	Unit	Note
E	191	GPa	Young's modulus
T_0	298	K	Reference temperature
ν	0.34		Poisson ratio (American Special Metals)
n	20		Hardening exponent (Healy et al. 2022)
m	1		Voce hardening parameter (Healy et al. 2022)
k	1.3806×10^{-20}	MPa mm ³ /K	Boltzmann constant
b	2.54×10^{-7}	mm	Burgers vector
θ_0	0.355	GPa	Initial hardening rate (Kocks and Mecking 2003)
μ_0	71	GPa	Shear modulus
D_0	0	GPa	Temperature dependence constant (Healy et al. 2022)
τ_a	0	GPa	Temperature and rate independent intrinsic yield strength
$\hat{\tau}_y$	123 (non-irradiated) 207 (irradiated)	MPa	Intrinsic yield strength
$g_{0,y}$	0.2		Constants related to activation energy barrier (Kocks and Mecking 2003)
q_y	2		
p_y	5		
$\varepsilon_{0,y}$ & $\varepsilon_{0,v}$	10^7	S ⁻¹	Reference strain rate
$\hat{\tau}_v$	20	MPa	Extrinsic yield strength
$g_{0,v}$	0.7		Constants related to activation energy barrier (Kocks and Mecking 2003)
q_v	2		

p_v	0.5		
ρ	7.9×10^{-3}	g/mm^3	Mass density

Through the iterative optimization process, $\hat{\tau}_v$ was determined to be 20 MPa for both the non-irradiated and irradiated materials. According to Equation 1, the maximum shear strength, $\tilde{\tau}$, can be calculated through the sum of τ_a , τ_y , and τ_v at the test temperature. Therefore, for the non-irradiated and irradiated samples, $\tilde{\tau}$ is approximately 122 MPa and 196 MPa, respectively, indicating an irradiation hardening by approximately 61%. Indeed, as reported by Nanstad et al. (Nanstad et al. 2009), the ultimate tensile strength of the HFIR irradiated 800H (580 °C, 1.28 dpa) increased from 463.9 – 535.4 MPa to 810.5 – 816.3 MPa, marking an approximate increase of 313 MPa or 62.8%. Although there is no unambiguous approach to correlate $\tilde{\tau}$ to UTS, the similar degree of irradiation hardening and the well-fitted simulation load-displacement curves in Figure 4 validate the parameters in Table 2.

TEM

The as-received material features a high density of dislocations, as can be seen in Figure 5 (a). The irradiation induced microstructural changes including small perfect loops, large Frank loops (edge-on or truncated), and precipitates, are visible in Figure 5 (b). Systematic $\mathbf{g} \cdot \mathbf{b}$ analysis was conducted to determine the burgers vectors of the small dislocation loops. It was found that the small dislocation loops are $\frac{1}{2}\langle 110 \rangle$ type perfect dislocation loops. The average size and volume number density of these loops were determined to be 3.3 ± 0.8 nm and $8.3 \pm 2.5 \times 10^{21} \text{ m}^{-3}$, respectively. Frank loops were imaged separately and the average size and volume number density were determined to be 156 ± 28 nm and $4.6 \pm 3.0 \times 10^{19} \text{ m}^{-3}$, respectively.

Figure 5 (c) shows the helium bubbles generated due to helium implantation, preferentially distributing along dislocations, grain boundaries, and phase boundaries between precipitates and the matrix. The micrograph was taken from approximately 4.5 μm away from the surface. The average diameter of the cavities are 4.1 ± 0.5 nm. Similarly, Zhu et al. has reported bubble size of 4.85 ± 0.53 nm in Alloy 800H after irradiation using 0.5 MeV He⁺ at 700 °C (Zhu et al. 2020).

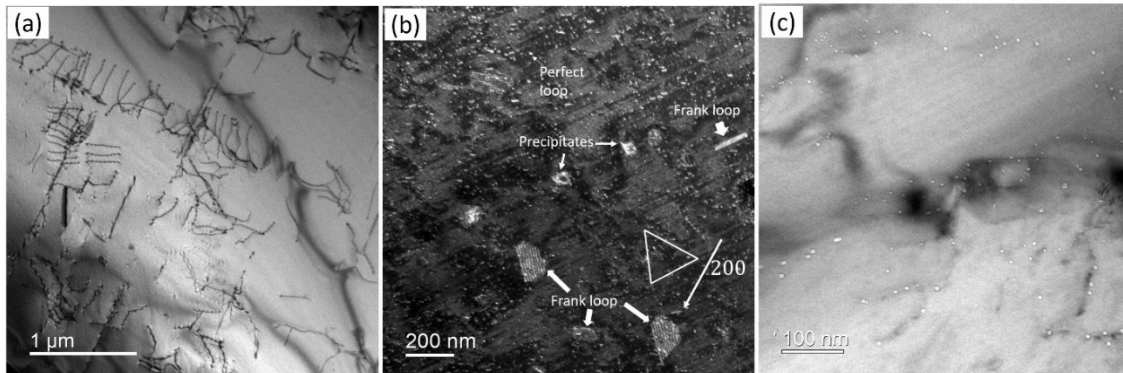


Figure 5 (a) TEM bright field micrograph showing dislocations in the non-irradiated material. (b) weak beam dark field (WBDF) micrograph taken in $g/5g$, $g = 200$ close to zone axis $[011]$ showing irradiation induced defects. The triangle indicates the three traces of the $\{111\}$ planes. (c) TEM bright field micrograph showing helium bubbles.

It has been reported that the irradiation induced damage and helium bubbles can significantly harden the material (Wang et al. 2022). The large dislocation loops especially Frank loops, precipitates, and helium bubbles can be strong obstacles to the movement of dislocations, which requires higher stress to overcome. The increment of yield strength after irradiation can be attributed to the presence of irradiation-induced damage. Additionally, the significantly increased yield strength along with the unchanged maximum work hardening stress, $\hat{\tau}_v$, in the CPFEM results, suggest that the work hardening rate was

reduced due to irradiation (WAS 2017). It is not clear whether work softening has happened due to dislocation channelling (Pokor et al. 2004). Therefore, further microstructure characterization of the deformed material is required.

CONCLUSION

In summary, the proton irradiated and helium implanted Alloy 800H demonstrated significant irradiation hardening. The hardness increased from 1.72 GPa to 2.66 GPa after 1 dpa, representing an increase from 312.31 MPa to 551.31 MPa in terms of the yield strength. TEM characterization revealed the generation of dislocation loops, precipitates, and helium bubbles, which are responsible for the irradiation hardening phenomenon. CPFEM based on open-source code has successfully simulated the nanoindentation experiment, through directly incorporating the experimental results.

ACKNOWLEDGMENTS

This research was funded by Atomic Energy of Canada Limited, under the auspices of the Federal Nuclear Science and Technology Plan. Computational resources for the work described in this paper were supported by the High-Performance Computing Cluster at Canadian Nuclear Laboratories.

REFERENCES

- American Special Metals. *INCOLOY Alloy 800H & 800HT*.
- Banerjee, Biswajit. 2007. "The Mechanical Threshold Stress Model for Various Tempers of AISI 4340 Steel." *International Journal of Solids and Structures* 44(3-4): 834-59.
- Bouzakis, K. D., and N. Michailidis. 2006. "An Accurate and Fast Approach for Determining Materials Stress-Strain Curves by Nanoindentation and Its FEM-Based Simulation." *Materials Characterization* 56(2): 147-57.
- Follansbee, P. S., and U. F. Kocks. 1988. "A Constitutive Description of the Deformation of Copper Based on the Use of the Mechanical Threshold Stress as an Internal State Variable." *Acta Metallurgica* 36(1): 81-93.
- Gan, J. et al. 2006. "Irradiated Microstructure of Alloy 800H." *Journal of Nuclear Materials* 351(1-3): 223-27.
- Hardie, Christopher D., Steve G. Roberts, and Andy J. Bushby. 2015. "Understanding the Effects of Ion Irradiation Using Nanoindentation Techniques." *Journal of Nuclear Materials* 462: 391-401.
- Healy, Brian et al. 2022. "WARP3D-Release 18.3.2." www.warp3d.net/%0Awww.github.com/rhdodds/warp3d.
- Hosemann, P. et al. 2009. "Nanoindentation on Ion Irradiated Steels." *Journal of Nuclear Materials* 389(2): 239-47. <http://dx.doi.org/10.1016/j.jnucmat.2009.02.026>.
- Kocks, U.F., and H. Mecking. 2003. "Physics and Phenomenology of Strain Hardening: The FCC Case." *Progress in Materials Science* 48(3): 171-273. <https://linkinghub.elsevier.com/retrieve/pii/S0079642502000038>.
- Lin, Pandong, Junfeng Nie, and Meidan Liu. 2020. "Study on Irradiation Effect in Stress-Strain Response with CPFEM during Nano-Indentation." *Nuclear Materials and Energy* 22(September 2019): 100737. <https://doi.org/10.1016/j.nme.2020.100737>.
- Mercier, David et al. 2015. "STABiX: A Matlab Toolbox for Slip Transmission Analysis." In *MTEX Workshop*.
- Nanstad, R. K. et al. 2009. "High Temperature Irradiation Effects in Selected Generation IV Structural Alloys." *Journal of Nuclear Materials* 392(2): 331-40.
- Nix, William D, and Huajian Gao. 1998. "Indentation Size Effects in Crystalline Materials: A Law for Strain Gradient Plasticity." *Journal of the Mechanics and Physics of Solids* 46(3): 411-25. <https://linkinghub.elsevier.com/retrieve/pii/S0022509697000860>.

- Pathak, Siddhartha, and Surya R. Kalidindi. 2015. "Spherical Nanoindentation Stress-Strain Curves." *Materials Science and Engineering R: Reports* 91: 1–36.
- Pokor, C. et al. 2004. "Effect of Irradiation Defects on the Work Hardening Behavior." *Scripta Materialia* 50(5): 597–600.
- Prasitthipayong, A. et al. 2018. "Indentation Size Effect in Unirradiated and Ion-Irradiated 800H Steel at High Temperatures." *Acta Materialia* 144: 896–904. <https://doi.org/10.1016/j.actamat.2017.11.001>.
- Rowcliffe, A. F., L. K. Mansur, D. T. Hoelzer, and R. K. Nanstad. 2009. "Perspectives on Radiation Effects in Nickel-Base Alloys for Applications in Advanced Reactors." *Journal of Nuclear Materials* 392(2): 341–52. <http://dx.doi.org/10.1016/j.jnucmat.2009.03.023>.
- Stoller, R. E. et al. 2013. "On the Use of SRIM for Computing Radiation Damage Exposure." *Nuclear Instruments and Methods in Physics Research, Section B: Beam Interactions with Materials and Atoms* 310: 75–80. <http://dx.doi.org/10.1016/j.nimb.2013.05.008>.
- Stoller, R. E. and S. J. Zinkle. 2000. "On the Relationship between Uniaxial Yield Strength and Resolved Shear Stress in Polycrystalline Materials." *Journal of Nuclear Materials* 283–287(PART I): 349–52.
- Takayama, Y. et al. 2013. "Nanoindentation Hardness and Its Extrapolation to Bulk-Equivalent Hardness of F82H Steels after Single- and Dual-Ion Beam Irradiation." *Journal of Nuclear Materials* 442(1-3 SUPPL.1): S23–27. <http://dx.doi.org/10.1016/j.jnucmat.2012.12.033>.
- Tan, Lizhen et al. 2019. "First Annual Progress Report on the Procurement and Post-Irradiation Examination of the Selected Samples of Alloy 800H and Grade 92 and 91 Steels." www.osti.gov.
- Toloczko, M. B. et al. 2018. "An Investigation of Microstructures and Yield Strengths in Irradiated Austenitic Stainless Steels Using Small Specimen Techniques." In *Effects of Radiation on Materials: 17th International Symposium*, 100 Barr Harbor Drive, PO Box C700, West Conshohocken, PA 19428-2959: ASTM International, 902-902–17.
- Topping, M. et al. 2023. "Design and Implementation of an Ion Beam Energy Degradation for Use in the Study of Nuclear Materials." *Journal of Nuclear Materials* 573: 154099.
- Wang, Qiang et al. 2018. "Orientation Dependent Evolution of Plasticity of Irradiated Zr-2.5Nb Pressure Tube Alloy Studied by Nanoindentation and Finite Element Modeling." *Journal of Nuclear Materials* 512: 371–84. <https://doi.org/10.1016/j.jnucmat.2018.10.033>.
- Wang, Qiang et al. 2022. "Characterization of Microstructure and Microhardness of Neutron Irradiated Inconel X-750." *Journal of Nuclear Materials* 563: 153644. <https://doi.org/10.1016/j.jnucmat.2022.153644>.
- Was, Gary S. 2015. "Challenges to the Use of Ion Irradiation for Emulating Reactor Irradiation." *Journal of Materials Research* 30(9): 1158–82.
- WAS, GARY S. 2017. *Fundamentals of Radiation Materials Science*. New York, NY: Springer New York. <http://link.springer.com/10.1007/978-1-4939-3438-6>.
- Xia, Y. Z. et al. 2014. "Synthesis, Characterization, and Nanoindentation Response of Single Crystal Fe-Cr-Ni Alloys with FCC and BCC Structures." *Materials Science and Engineering: A* 611: 177–87.
- Zaafarani, N. et al. 2006. "Three-Dimensional Investigation of the Texture and Microstructure below a Nanoindent in a Cu Single Crystal Using 3D EBSD and Crystal Plasticity Finite Element Simulations." *Acta Materialia* 54(7): 1863–76.
- Zhu, Zhenbo, Hefei Huang, Awen Liu, and Zhiyong Zhu. 2022. "Quantitative Characterization of Frank Loops and Their Effects on the Plastic Degradation in Heavy Ion Irradiated Alloy 800H." *Materials Science and Engineering: A* 832(December 2021): 142501.
- Zhu, Zhenbo, Hefei Huang, Jizhao Liu, and Zhiyong Zhu. 2020. "Helium-Induced Damage Behavior in High Temperature Nickel-Based Alloys with Different Chemical Composition." *Journal of Nuclear Materials* 541.